An artificial intelligence classifier for electron beam powder bed fusion as-built surface topographies

An artificial intelligence classifier for Electron Beam Powder Bed Fusion as-built surface topographies

Giacomo Maculotti[*1], Cristian Ghibaudo[2], Gianfranco Genta[1], Daniele Ugues[2], Maurizio Galetto[1]

[1]Department of Management and Production Engineering, Politecnico di Torino, C.so Duca degli Abruzzi 24, 10129, Turin, Italy

[2]Department of Applied Science and Technology, Politecnico di Torino, C.so Duca degli Abruzzi 24, 10129, Turin, Italy

[*]Corresponding author. email: giacomo.maculotti@polito.it

HIGHLIGHTS

- PBF components as built topography depends on internal defects and process parameters.
- Topographies are quantitatively characterised by a large set of complex parameters.
- In-situ controls are based on qualitative inspection.
- An ML-algorithm is developed to visually classify topographies based on parameters.
- The tool will allow multi-scale, information-rich automated quality control for AM.

ABSTRACT

Additive Manufacturing, a pillar of Industry 4.0, to enable automatic real-time process control, relies on in-situ measurements, some of which - currently under development - exploit surface topography. Topographic characterisation requires a large set of parameters, loosely linked to visual appearance upon which related in-situ measurements are mostly based. A supervised machine learning classifier of as-built surfaces based on topographical characterisation is proposed and applied to tool steel test pieces fabricated by electron beam powder bed fusion. The methodology is developed to provide process engineers with the visual appearance of the topographical parameters set, and enable multi-scale, information-rich quality control.

Keywords: Surface topography, Machine Learning, feature characterisation, classification, Electron Beam Melting, quality control

1. INTRODUCTION

Additive manufacturing (AM) is one of the pillars of Industry 4.0 [1,2] and will have a core role in the future of the manufacturing industry [3]. Provided its capability of producing highly customised components both from a geometrical and material composition perspective [4], AM allows definitive optimisation of energy and raw material consumption, thus being essential in the Green Deal and circular economy framework [5–7]. Amongst the several AM techniques, powder bed fusion (PBF) processes are the most investigated in the literature, exploited in industry, and the ones with greater technological readiness [8,9]. Electron beam melting (EBM or EB-PBF) is one PBF process massively exploited in industry and academia [10].

In this technique, electrons are generated by a tungsten filament or a lanthanum hexaboride cathode and accelerated to 60 keV. Then two electromagnetic lenses focus and deflect the beam onto the powder bed [11]. The overall process can be divided into three main stages: i) pre-heating of the start plate, ii) building of the component, and iii) cooling helped with He flux. During the melting, the process is undertaken in a controlled vacuum (10^{-4} mbar) thanks to a small helium pressure to prevent so-called smoke events. During the building of each layer, it is possible to identify four steps: i) application of a homogeneous powder layer supplied by two hoppers located on the side above the building tank and distributed by the movement of a stainless steel rake; ii) pre-heating of the powder bed, during which the powder particles are slightly sintered in order to enhance the electrical conductivity of the powder bed and ensure stability to the process; this step allows regulating the building temperature, which depends on the processed material; iii) melting step, during which

the electron beam is focused on the powder bed, and the scanning speed is reduced with respect to the pre-heating step to melt selected area to create the final component; iv) the last step, to compensate the total energy used in the process: in this step, the electron beam is used to regulate the temperature of the build with the same process parameters as of the pre-heating in order to remain at the selected build temperature [11,12].

Process parameters influence parts' final quality and characteristics. The relative density of the final components mostly depends on the melting parameters and on the quality of the powder [12]. Amongst the melting parameters, the melting strategy, the beam power, which depends on the voltage and the beam current, the scanning speed and the line offset of adjacent lines are the most relevant. Guo et al. [13] reported that the relative density of Ti-6Al-4V specimens produced by EB-PBF is inversely proportional to scanning speed and directly proportional to the beam current. Additionally, they showed a qualitative dependence of the top surface on the internal porosity [13]. Wang et al. [14] considered two alternative melting strategies, i.e. multi-beam and continuous beam, and their influences on the surface roughness. The main advantages of the EB-PBF process on L-PBF lie in the vacuum environment and the higher achievable building temperatures. The vacuum environment enables processing material with lower interstitial element content [15]. The high building temperature reduces the thermal gradient and, consequently lowers the residual stresses in the component. In fact, the final residual stresses are generally lower than those characteristics of L-PBF process [16]. This allows the processing of materials more sensitive to thermal crack formation, like poorly weldable alloys, medium to high alloyed steels, and strongly precipitation hardened Ni superalloys [15,17–21]. On the other hand, the wider Powders Size Distribution (PSD) and the larger average size of powders that are used in EB-PBF with respect to those used in L-PBF indeed result in poorer surface finish. Currently, this is a drawback of the considered manufacturing process that users have to accept.

The technological readiness and the flexibility of the EB-PBF process make it interesting to design highly customised designs in terms of material composition and geometry for industrial applications [8,9]. Nowadays, EB-PBF can process several materials [12,15,19], and some automotive and aerospace industrial applications are already available, especially for Ti alloys and TiAl alloys [22]. Moreover, the characteristic of EB-PBF opens to the processability of a new range of materials for which the traditional processes show severe limitations, e.g. refractory materials [20,21] and high entropy alloys (HEAs) [23]. Therefore, it is crucial to employ fast, economical, and reliable techniques to accelerate the optimisation of the process parameters.

Accordingly, a consistent amount of literature has focused on inferring correlations between process parameters and part properties, such as microstructure [24,25], porosity [26], mechanical properties [24,27], and surface finish [28]. Consistently, the maturity of the process and the need for integration and automation typical of the current manufacturing pushed the development of a quality control system for PBF processes. These typically rely on multi-sensor techniques and exploit the big data availability [9]. Different quality control techniques are available, ranging from off-line to in-situ characterisation techniques [29]. Off-line controls, e.g. SEM microstructure characterisation [30,31], nano-indentation [32–34] and XCT [35,36], are typically highly informative but not suitable for feedback closed-loop process controls as they are off-machine and sometimes destructive and expensive. Conversely, in-situ controls are in-process and on-machine, enabling quick decision-making and process control. These will ultimately enable the complete automation of AM processes and subsequent finishing steps in the years to come. In-situ quality controls target quantities that can be measured during the process and directly correlated to part properties. The measurements of observable features can be divided into five levels, as reported in Table 1 [9].

Table 1. In-situ measurements techniques for on-line quality control of PBF processes.

Level	Process signature	Characteristics
0	Environmental characteristics of AM system (chamber pressure, temperature, oxygen content, inert gas flow, etc.)	AM-machine embedded sensors; high-frequency acquisition, raw signals.
1	Powder bed homogeneity, geometrical characteristics, and topography of the layer.	Additional sensors, measuring at least once per layer the build area or a region of interest.

2	Scan track, interaction between powder and beam, spatial thermal field history, local defects (spatters, plume emissions).	Additional sensors, high frequency, and high spatial resolution.
3	Melt pool characteristics (stability, shape, size, physical and thermodynamic state).	Additional sensors, high frequency and highest spatial resolution.
4	Under the layer measurements (melt pool depth, sub-surface defects, etc.)	Additional sensors (ad-hoc prototypes).

Surface topography measurements have been introduced recently among the several in-situ measurements and monitoring methods. Surface topography measurements are Level 1 monitoring techniques and represent the most recent technical development of optical surface topography measuring instruments. Surface topography, i.e. the geometrical feature that interacts with the surrounding environment, consists of the component's shape, texture, and surface features [37]. The topographical characterisation is essential when designing and optimising processes, materials, and components because it controls many properties, thus ultimately contributing to the part's final quality [38]. Properties that can be controlled include optical, biological, e.g. adsorption, mechanical, e.g. hardness, and tribological properties, e.g. stiction and wear. Consequently, surface technologies and careful process parameters tuning have been exploited to engineer the topography and control the resulting properties and functionality [39,40]. Consistently, extended research can be found correlating process parameters, topography, and components' properties both in conventional and AM-PBF processes [28,40–42]. In particular, focusing on EB-PBF, topography resulted in being mostly affected by beam speed and current, laser offset and focus [9], and part build geometry [43]. Similarly, the topography is related to porosity and mechanical properties [41]. In fact, literature both qualitatively and quantitatively have highlighted how internal defects, e.g. porosities or irregularities, might propagate to outer layers introducing severe topographical irregularities in the top surface, up to warping the overall part [44–46]. Therefore, academia and industry have recently been developing measuring systems that can achieve in-situ surface topography measurements. They can be based on several technologies, i.e. fringe projection systems [47,48], focus variation [49], blade mounted sensors [50], co-axial coherent imaging [51,52], and electronic imaging [53,54]. The first two are technologies native for surface topography measurements with high-end metrological characteristics and measurement flexibility [47,55]. The blade-mounted sensors measure topography as a secondary result of other acquisitions, resulting in a cheaper implementation but with poor metrological performance and limited topographical feature measurement capabilities, e.g. for elevated edges [9]. The last two exploit the processing system to obtain topographical measurements. They are peculiar for L-PBF and EB-PBF processes, respectively. However, despite the structural and design advantages, they feature a limited lateral resolution, only allowing the characterisation of coarser topographical features.

State-of-the-art applications of Level 1 in-situ topographical measurements are devoted to detecting localised defects, i.e. topographical features, [9,56] and feeding information to the closed-loop process control [57]. This is achieved by either exploiting the formerly discussed topographical measurements [9,56] or relying upon 2D images [58,59]. It is clear that the former are more informative, are traceable, and would allow, at once, quantitative characterisation through surface topography parameters [60]. However, despite the mentioned advantages and the literature exploiting area field parameters (*Sa*, *Sq*, etc.) [60] to qualify and optimise the manufacturing process, these are rarely adopted for in-line quality control. Conversely, literature presents quality controls based on small scale topographical characterisation, i.e. feature-based characterisation [9,56,61]. The reasons for this are manifold. AM topographies require complex characterisation that must include both conventional texture and advanced feature characterisation [43,62]. It results in a large set of parameters to be evaluated and managed. Moreover, the interpretation of this set is often challenging and not straightforward. In fact, although the meaning of each parameter is clear, the indication of the geometrical resemblance of the topography by the set can be elusive for not highly experienced practitioners in topographical characterisation. Conversely, visual information can be utmost useful for process designers. Literature has formerly attempted a classification of the most frequent geometrical resemblance of as-built EB-PBF topographies. They typically include, for non-optimised processes, the distributed presence of topographical features, i.e. globules and surface pores, or an *orange peel* aspect; for optimised processes, the

possible presence of isolated topographical features or a clean topography [13,44,45,62,63]. Literature performs topographical classification and discusses correlation with other defects based on visual qualitative aspects [13,63]. However, the literature does not address the relationship with surface parameters used for geometrical dimensioning and tolerancing (GD&T) specification.

This work develops a tool based on a supervised machine learning (ML) algorithm to classify EB-PBF as-built topographies based on state-of-the-art topographical quantitative characterisation. The resulting classification aims to provide a visual indication of the meaning of the set of topographical characterisation parameters to aid process engineers and quality practitioners in the design. Moreover, when coupled with quantitative characterisation, these visual indications will allow multi-scale, information-rich quality control [64,65], which is essential on the route towards an integrated multi-sensor automated control system for AM. In fact, recalling the mentioned correlation between process parameters, component properties, and the surface topography, an integrated and automated control system could be conceived to trigger process parameter modification to optimise the part build, the interruption of the manufacturing process if the part would result defective, and the selective execution of some post-processing to optimise costs. The rest of the paper is structured as follows. Section 2 discusses the considered materials and methods and presents the state-of-the-art as-built EB-PBF surface topography characterisation and classification. Section 2 also presents the methodology to build the proposed supervised ML algorithm to classify the topographies. The methodology is applied to the case study of industrial relevance (i.e. an H13 by EB-PBF, formerly introduced); relevant results are presented and discussed in Section 3. Finally, Section 4 draws conclusions.

2. MATERIALS AND METHODS

This section describes the scope of the work in terms of the considered material in subsection 2.1. Then it addresses the applied methodology for topographical measurement and characterisation (subsection 2.2) and presents the proposed supervised machine learning algorithm for the classification of surface topography based on surface topography parameters.

2.1 Sample preparation

In the present work, an AISI H13 fabricated via EB-PBF was considered. Additive fabricated AISI H13 tool steel is mainly studied to produce moulds and dies with conformal cooling for hot forming and die casting [66,67]. The significant content of carbides in the tempered martensite matrix provides high hardness and wear resistance at elevated temperatures, while the low cost makes this material widely used in the industrial sector. Although the conventional route for producing AISI H13 components is well established, AM route offers many advantages, e.g. novel design of conformal cooling dies [67,68]. Many works on AISI H13 manufactured by L-PBF are present in the literature [69–76]. Although some attempts to reduce the crack formation in the component produced by L-PBF by heating the start plate have been accomplished [75,76], the crack susceptibility of this material hinders the processing via L-PBF of crack-free components. Conversely, the higher pre-heating temperature easily obtainable in EB-PBF allows producing dense and crack-free components once the melting parameters have been optimised. AISI H13 produced by EB-PBF was initially studied by Cormier et al. [77], where a first set of process parameters is reported.

In the present work, 52 cubic specimens of 30 mm of lateral dimension have been produced on a 304 stainless steel start plate with an ARCAM A2X system. The starting powder was a gas atomised AISI H13 powder with EB-PBF particle size distribution (35-150) µm. The electron beam followed a snake-like scanning pattern with a rotation of 90° after each layer. The melting process parameters were varied in a wide range, i.e. the energy density from 15 J/mm^3 to 120 J/mm^3, mainly modifying the beam speed from 300 mm/s to 3200 mm/s [78]. Other modified process parameters were the beam current, on two levels (8 mA and 15 mA), the line offset from 0.2 mm to 0.3 mm, and the focus offset from 15 to 35 mA [46]. The pre-heating temperature was set at 700 °C. Therefore, different conditions, both inside and outside the process window, are considered to generate a comprehensive set of surface aspects.

2.2 Topography characterisation of components by EB-PBF

Surface topography characterisation is standardised by the ISO 25178 series within the GPS framework. The topography can be thought of as the result of the superimposition of several structures at different length scales, i.e. different spatial wavelengths. These include roughness at low scales, form at large scales, and waviness, i.e. a periodic structure typically at large scales. Additionally, some individual elements, i.e. topographical features, can be present [43,62].

2.2.1 Main categories of EB-PBF topographies

In this paper, the discussion is limited to upward-facing surfaces because they are the only accessible by Level 1 in-situ measurement. Consistently, as-built, i.e. not finished nor post-processed, surfaces are considered, as motivated in the introduction, to refer to in-situ measurements [9]. Figure 1 shows some examples of the main types of EB-PBF as-built topographies.

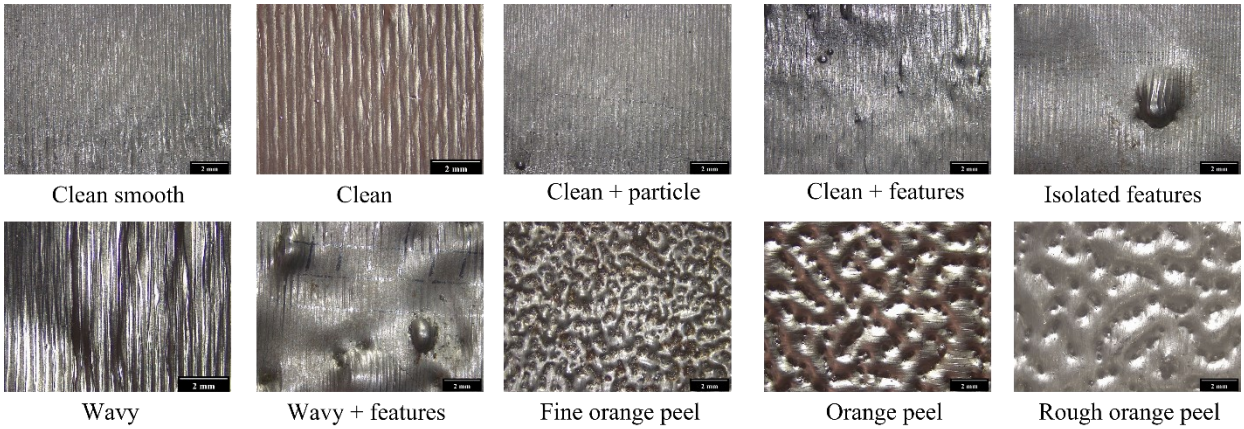

Figure 1 Main categories of EB-PBF as-built topographies. As-built top surfaces of H13 by EB-PBF. Images were taken with a LEICA stereomicroscope, 8× magnification. Scale bar: 2 mm.

Top as-built surfaces of components by EB-PBF with parameters inside the process window and in the neighbourhood of the optimal point are typically clean. Both roughness and micro-scale waviness can be present. The roughness is typically due to the interaction between the electron beam and the powder particles [62]. Clean surfaces allow appreciating micro-scale periodic texture due to the line offset and the scanning strategy of the electron beam with a varying degree of smoothness that depends on the process parameters, that can reach a waviness scale [45]. Sub-optimal process parameters may induce a Marangoni flow, generating features resembling the melted tracks, which result in significant waviness [62].

Conversely, in the case EB-PBF process parameters are not inside the process window, the presence of topographical features dominates the resulting topographies. Mostly, two main cases can be distinguished. If the energy input is insufficient, which can be due to excessively high scanning speed, the melted track is not continuous. This results in internal porosities and defects that create several dales, or surface pores, leading to the so-called *orange peel* topography [13,44,45,62,63]. Alternatively, extreme process conditions may promote uneven dynamics of the melt pool, i.e. overheating and movement of the liquid, generating a swollen topography, that is, a topography dominated by a globule, i.e. a protruding feature.

Indeed, intermediate process conditions, i.e. non-optimised parameters inside the process window, can generate wavy topographies with large, isolated features, including dales and globules [44,45]. Last, regardless of process parameters, sputter particles can also be present, which are globules from the perspective of topographical characterisation and can be interpreted as isolated features.

2.2.2 Characterisation methodology of EB-PBF topographies

Because of the complex appearance and presence of multiple spatial scales, thorough EB-PBF topographies characterisation requires a combination of areal field parameters and feature parameters [43,60,62,79]. This section briefly describes the characterisation methodology applied in this work, according to the literature and standard best practices.

Literature and standards require separating the length scales for analysis, namely form, waviness, and roughness [43,60,62]. The characterisation of AM as-built topographies can focus on waviness surfaces. In fact, it includes both the manufacturing signature and, possibly, some additional features [62], as discussed in the previous section. The first step to isolating the waviness surface is to remove the possible macro-geometric error of planarity by applying the F-operator. Ultimately, this operation removes from the measured topography the least-square-fitted surface modelling the nominal form. This operation requires prior removal of measurement disturbances, i.e. non-measured points and spikes [80].

Secondly, the residual topography of the F-operator can be studied to achieve topographical characterisation. Standard filters have to be applied to extract the waviness. The filter type is discussed in the following, referring to the spatial wavelength domain. Initially, measurement noise is suppressed by applying an S-filter, i.e. a high-pass filter. A robust Gaussian filter is a convenient choice among the several available filters, for it is inherently robust to measurement disturbances [81,82]. The nesting index of the S-filter depends on the measurement set-up and is standardised by the ISO 25178-3:2012 [81]. Once the noise has been removed, the waviness surface can be extracted. This can be achieved by applying a high-pass robust Gaussian filter [62]. The selection of the most appropriate nesting index is crucial. In fact, wrong dimensioning is liable to remove topographical features relevant to the manufacturing signature. Therefore, differently from the most common standard prescription [81], the choice must be made considering the power spectrum density of the topography heights [62,83]. In particular, multi-scale sensitive analysis can be resorted to [37], and, in this work, fractal analysis is exploited [37,60,84]. This type of analysis is exploited in literature to study the wavelengths of topographies and relate them to the manufacturing process [85]. The multi-scale fractal analysis seeks the size of periodical structures to model the measured topographies at different scales. Fractals are continuous but nowhere differentiable functions with self-similarity, or affinity, properties. Technological surfaces show self-affinity because they seem smooth at large observation scales and rougher at lower observation scales. In particular, roughness can be interpreted as a geometrical irregularity that can be modelled by fractals [37]. Changing the observation scale, i.e. the fractal dimension, different degrees of approximation can be obtained. The scale at which the roughness can be appreciated is the smooth-to-rough-crossover (SRC) [37,84], which can be consistently chosen as the nesting index to extract the waviness surface.

Finally, the resulting extracted waviness surface and roughness surface, i.e. the SL-Surface, can be characterised. The waviness surface characterisation requires evaluating topographical areal field parameters, e.g. the arithmetical mean height of the surface *Sa*, the root mean square height surface *Sq*, the root mean square gradient of the surface *Sdq*, and feature parameters [60]. The SL-Surface requires, to begin with, feature identification. This can be obtained by watershed segmentation [60]. This is a technique conceived for geography and successfully applied in technological surfaces characterisation [37,86], which separates a topography into smaller regions. The method supposes that the topography is flooded with rain and that, in such a condition, water flows downwards steepest paths to domains of attractions [37,62]. The watersheds are lines that segment the topography in regions that represent subsequent water catchment basins. Literature has recently improved the method by applying it to surface height gradient maps, obtained by a Sobel operator, rather than on the height map itself. This increases the accuracy and robustness of the watershed segmentation by enhancing the edges of topographical features [43,62,87,88]. Additionally, watershed segmentation is known to suffer from over-segmentation. Therefore, pruning is necessary [37,60]. Effective pruning for EB-PBF topographies can be obtained by applying a threshold of three times the standard deviation above and below the average height to identify respectively hills and dales [88]. Once the topographical features have been identified, feature characterisation is carried out. This includes evaluating for both globules, i.e. hill, and surface pores, i.e. dale, the overall volume (V_g and V_p) and the area percentage to the whole surface ($A_{\%g}$ and $A_{\%p}$) [62].

Namely, the identified features can be removed to allow the characterisation of the *actual* roughness surface through areal field parameters, e.g. *Sa*, *Sq*, *Sdq*, *Ssk*, *Sku* [62]. However, in the case of an orange-peel topography, i.e. completely dominated by surface pores, it is apparent that not enough data would remain to perform such characterisation. Therefore, in this work, roughness surface is not considered. Table 2

summarises the topographical parameters that are exploited to characterise EB-PBF as-built topographies in this work.

Table 2 Topographical parameters exploited to characterise as-built EB-PBF topographies.

Parameter	Evaluation Surface	Parameter type
SRC	S-Surface	Field
Sa Sq Sdq	Waviness surface	
V_g $A_{\%g}$ V_p $A_{\%p}$	SL-Surface	Feature

2.2.3 Measurement set-up of EB-PBF topographies

The specimens' top surface was measured by a state-of-the-art surface topography measuring instrument based on coherence scanning interferometry (CSI) [89,90], namely a Zygo NewView 9000. Measurements were set up to trade-off between metrological performances and time. Accordingly, measurements were performed exploiting a 5.5× Michelson objective lens with a numerical aperture of 0.15, a digital zoom 0.5×, resulting in a pixel size of 3.15 μm. Stitching of 4×4 fields of view, each of (1000×1000) pxl, was applied to obtain an investigated area of (13×8) mm; the longer size was set orthogonal to the scanning tracks. The investigated area is thus chosen significantly larger than what literature considers to be sufficient to obtain representative characterisations, i.e. ~(5×5) mm [43,62,87,88]. Measurements were obtained as the average of 4 replications to reduce noise, with the application of signal oversampling to improve the signal-to-noise ratio in regions challenging to be measured [91]. Measurements were performed in the top region of the specimens at a distance of 3 mm from each edge. In so doing edges are excluded from the measurement, consistently with their liability of introducing singularities in the topography. Considering the investigated large area and the uniformity of the topographies, as it can be appreciated in Figure 1, a single location is deemed representative. Samples manufactured in the most extreme conditions, which resulted in the most irregular topographies, were additionally measured at the centre of the top surface. These further data are introduced in the dataset to increase the training set numerosity and representativeness, resulting in 77 data.

Current state-of-the-art surface topography measuring instruments are only at a research and prototype stage for in-situ measurements. The performed measurements are ex-situ. This work aims to develop a methodology and model easily applicable to the in-situ surface topography measurements currently being developed [47–49]. Whilst CSI technology is not the best choice for in-chamber installation and other surface topography measurement techniques are, e.g. fringe projection [47,48], focus variation [49], CSI is the most accurate topographical measurement method [92,93], thus is considered in this work to present and demonstrate the proposed classification method.

Measured surface topographies are characterised according to the methodology formerly discussed; the S-filter nesting index was set to 10 μm [81]. The characterisation has been performed using the commercial state-of-the-art software MountainsLab v8.0. Moreover, mid- to high-magnification imaging by SEM of the measured regions was performed to obtain further qualitative information on the measured topographies' morphology and the defect types.

2.3 Supervised machine learning for topography classification

This section describes the chosen classifier architecture and algorithm and the methodology to train it and optimize its hyperparameters.

Classification problems intend to define classifying criterion $\mathcal{C}$ that can associate a class label $y \in \{C_1, \dots, C_n\}$, where n is the number of classes, to a set of inputs $\boldsymbol{x}$, such that $y = \mathcal{C}(\boldsymbol{x}, \boldsymbol{\vartheta})$, where $\boldsymbol{\vartheta}$ is the set of hyperparameters of the model [94]. In the present work, n = 10, according to Section 2.1, and $\boldsymbol{x} \in \mathbb{R}^{1,8}$, according to Table 2. The classification is a supervised machine learning problem because the classifying criterion is defined based on a training set $\mathcal{L}$ of N-tuples of $(\boldsymbol{x}, y)$, which has been formerly labelled by a supervisor, and aims to predict the class of a new set of input, i.e. to achieve a generalisation [94]. The problem has been well defined and studied in the literature since the introduction of logistic regression. It consists in finding the functional form of $\mathcal{C}$ and the related $\boldsymbol{\vartheta}$ that minimise a loss function, $f = f(y,\ \mathcal{C}(\boldsymbol{x}, \boldsymbol{\vartheta}))$, based on a training set of input data, and optimise the prediction accuracy, i.e. the ratio of correct prediction to the size of the set or the complement to one of the misclassification rate [94]:

$$Acc(\mathcal{C}, \mathcal{L}) = 1 - \frac{1}{N}\sum_{i=1}^{N} \mathbb{I}(\mathcal{C}(x_i) \neq y_i) \quad (1),$$

where $\mathbb{I}(x)$ is the indicator function, so that $\mathbb{I}(x) = 1$ if x is true, otherwise is $\mathbb{I}(x) = 0$. As the interest lies in the generalisation capabilities of the model, typically, the accuracy is also evaluated on a test set, i.e. a sample independent from the training set. The latter can be obtained by bootstrap or constrained bootstrap sampling the training set. In this work, cross-validation is considered, which consists in splitting in k folds the data set. Each fold, in turn, is used as a test set. In so doing, each point is predicted once and used to build the classifier k-1 times. The accuracy is computed as the average accuracy of all the folds [94]. In this work, 5 randomly generated folds are considered, in line with common best practices [94]. Thus, the dataset of 77 measurements was randomly split into 5 groups, 3 of 15 data and 2 of 16, and training and cross-validation are performed accordingly.

Literature offers several choices of supervised machine learning classifiers, ranging from parametric approaches, e.g. logistic regression [94], to non-parametric models, e.g. classification and regression trees (CART) [95], ensembles of trees [96,97], support vector machines (SVM) [98].

CART classifiers describe a decision rule that a tree can graphically represent; each branch node is a decision rule that leads to a leaf which is the class. Trees' main parameters are the depth, i.e. the number of nodes on the same branch, and the width, i.e. the number of branches. A particular way to construct decision trees is boosting. This algorithm applies the weak learner to a weighted version of the data many times to optimise a certain loss function. Greater weights are associated with misclassified points to improve the accuracy [99]. In general, trees suffer from excessive growth, making them hard to interpret and liable to overfit the data [94]. Several alternatives to relieve this issue are available. Amongst them, creating an ensemble of weak learners is particularly effective [96,97]. By aggregating several simpler weak learners, ensembles result in greater simplicity, robustness, and accuracy. The decision rule across the weak learners is typically by a simple majority. Consequently, in addition to the parameters typical of the weak learner, the base learner numerosity and the method to create their several instances define the ensemble. Bootstrap aggregating, i.e. bagging, allows creating an ensemble of trees by taking bootstrap samples $\mathcal{L}_B$ of m data from $\mathcal{L}$, drawn randomly with replacement, and exploiting each of them to create a weak classifier $\mathcal{C}_B$ [96]. If the input data and the data dimension are subsampled with the same methodology, a random forest can be obtained. This solution has the advantage of constructing uncorrelated predictors for the different samples $\mathcal{L}_B$ [94,97].

A support vector machine is a machine learning classification algorithm that maps the input data in hyperspace and defines a hyperplane that can identify two groups of data, i.e. it allows binary classification [98]. SVM allows, by space transformation, the solution for nonlinear classifiers, i.e. the identification of hypersurfaces nonlinear in the original hyperspace that in the transformed space are hyperplanes [94]. Strategies are available to solve also multi-classification problems. The main parameters of an SVM are the parameters describing the hyperplanes and the tolerance ϵ. This defines a tolerance around the hyperplane for the classification. The support vectors are the observed points that lie on the boundary of the separating hyperplane, whose parameters are obtained by solving a quadratic dual problem [94,100].

Non-parametric approaches, e.g. CART and SVM, are more flexible and yield more robust and accurate classifiers, although selecting the best set of hyperparameters is more complex [94]. In fact, due to the several parameters and their highly nonlinear effect on accuracy, optimisation in closed-form solutions is often expensive. A convenient alternative methodology exploits black-box models between the hyperparameters $\boldsymbol{\vartheta}$ and the accuracy, $Acc = Acc(\boldsymbol{\vartheta})$, and maximises the classifier accuracy by Bayesian optimisation algorithm [101] by finding $\boldsymbol{\vartheta}_{best} = \underset{\boldsymbol{\vartheta}}{\operatorname{argmax}}(Acc(\boldsymbol{\vartheta}))$. The approach is computationally less demanding and is demonstrated to achieve a global optimisation [102]. The Bayesian optimisation assumes that the unknown cost function describing the model accuracy, $Acc(\boldsymbol{\vartheta})$, is a real Gaussian Process (GP) realisation, which provides suitable flexibility and regularity to the function. A prior distribution of the GP is hypothesised and iteratively updated, through the posterior distribution, obtained as new observation of the function are made. Consequently, the choice of the new evaluation point, $\boldsymbol{\vartheta}_{next}$, of the cost function is crucial in the algorithm, for it determines the posterior. The selection of $\boldsymbol{\vartheta}_{next}$ is made by studying a certain acquisition function, $a = a(\boldsymbol{\vartheta}^*; \boldsymbol{\vartheta}, \{(\boldsymbol{x}, y)\})$, such that $\boldsymbol{\vartheta}_{next} = \underset{\boldsymbol{\vartheta}^*}{\operatorname{argmax}}(a)$ [101,103]. The literature proposes several alternative acquisition functions. One of the criticalities is defining a suitable trade-off between the exploitation and the exploration of the hyperparameter space. In particular, the acquisition function has to guarantee that regions that minimise the cost function are thoroughly investigated, i.e. exploited, and that those with higher uncertainty, i.e. little explored, are appropriately investigated. Amongst the others, the *constrained overexploitation expected improvement per second* is a suitable choice that allows achieving a global optimisation considering the computational effort [101,103]. In particular, the method assumes the acquisition function as:

$$a_{EIpS}(\boldsymbol{\vartheta}^*; \boldsymbol{\vartheta}, \{(\boldsymbol{x}, y)\}) = \frac{\mathbb{E}\left[\max\left(0, \mu_Q(\boldsymbol{\vartheta}^*) - Acc(\boldsymbol{\vartheta})\right)\right]}{\mu_S(\boldsymbol{\vartheta}^*)} \tag{2},$$

where $\mu_Q(\boldsymbol{\vartheta}^*)$ is the minimum posterior mean and $\mu_S(\boldsymbol{\vartheta}^*)$ the posterior mean of the GP model describing the evaluation time. Under the assumption that the accuracy distributes as a GP model with a predictive mean $\mu(\boldsymbol{\vartheta}^*; \boldsymbol{\vartheta}, \{(\boldsymbol{x}, y)\})$ and predictive standard deviation $\sigma(\boldsymbol{\vartheta}^*; \boldsymbol{\vartheta}, \{(\boldsymbol{x}, y)\})$, Eq.(2) becomes:

$$a_{EIpS}(\boldsymbol{\vartheta}^*; \boldsymbol{\vartheta}, \{(\boldsymbol{x}, y)\}) = \frac{\sigma(\boldsymbol{\vartheta}^*; \boldsymbol{\vartheta}, \{(\boldsymbol{x}, y)\}) \left(\gamma(\boldsymbol{\vartheta}^*)\Phi\left(\gamma(\boldsymbol{\vartheta}^*)\right) + \mathcal{N}(\gamma(\boldsymbol{\vartheta}^*); 0,1)\right)}{\mu_s} \tag{3.1}$$

$$\gamma(\boldsymbol{\vartheta}^*) = \frac{Acc(\boldsymbol{\vartheta}_{best}) - \mu(\boldsymbol{\vartheta}^*; \boldsymbol{\vartheta}, \{(\boldsymbol{x}, y)\})}{\sigma(\boldsymbol{\vartheta}^*; \boldsymbol{\vartheta}, \{(\boldsymbol{x}, y)\})} \tag{3.2},$$

where $\Phi\left(\gamma(\boldsymbol{\vartheta}^*)\right)$ is the standard normal density function [101,102]. Additionally, the posterior standard deviation must not be smaller than a certain fraction of the prior standard deviation. This constraint avoids overexploitation, i.e. finding local minima. In fact, if it is not satisfied, the new hyperparameters set $\boldsymbol{\vartheta}_{next}$ belongs to a region with a small uncertainty, i.e. it is between already tested points. If that is the case, a multiplication factor proportional with a factor multiple of 10 to the number of performed iterations of the Bayesian algorithm is applied to the $\boldsymbol{\vartheta}_{next}$ to correct the next evaluation point [102]. Bayesian optimisation with 45 iterations is applied; the number of iterations is slightly greater than the empirical suggestion of 30 [94].

In this work, the classifier shown in Figure 2 is proposed, where topographical classes are taken from the literature, as discussed in Section 2.2. The classifier operates in two steps to additionally identify the adequacy of the adopted process parameters. Figure 3 shows scatter plot of process parameters clustered on the basis of the classification proposed in Figure 2. Here, main processing parameters typically reported in literature are considered for sake of discussion, i.e. the electron beam power *P*, the line energy *LE*, i.e. the ratio between *P* and the scanning speed *v*, and the area energy *AE*, i.e. the ratio between *LE* and the line offset. Those parameters are mainly controlling the topography and the generation of other defects [46]. Accordingly, considering surface topography quality as per Section 2.2, processing parameters in-process and out-of-process window can be identified. The latter are related to swollen topography, i.e. with isolated features and severe waviness leading to orange peel. The former could be further split, basing on additional material properties, e.g.

mechanical response, internal defect content to highlight optimized process condition, i.e. related to low power and low speed (see Figure 3). This is consistent with literature reviewed in Section 2.2, for it allows optimizing the surface avoiding excessive waviness, introduced by higher speed, and swelling, due to excessive energy. Therefore, the proposed classifier consists of a convolution of three classifiers $\mathcal{C}_1$, $\mathcal{C}_2$ and $\mathcal{C}_3$, each of which has to be trained according to the methodology formerly discussed. $\mathcal{C}_1$ performs a binary classification to highlight the process parameter adequacy and is selected as an SVM algorithm. This choice is preferred to other typical binary solutions, e.g. logistic regression, because it has to be applied in a large hyperspace and features more flexible kernel functions to model non-linearity between the features [94]. Because at the considered level only surface topography information are available, and in general if a new material is investigated, relationship between other properties may be unavailable, the further distinction between in-process window and optimized process in not considered. The Bayesian optimisation will target the kernel function (considering among the alternatives linear, quadratic, and gaussian kernels) and the tolerance ϵ. Sequentially, basing on the output of $\mathcal{C}_1$, the other classifier, i.e. either $\mathcal{C}_2$ or $\mathcal{C}_3$, is applied to achieve the actual topographical classification. The other two classifiers are chosen as tree classifiers to better fit the larger number of available classes. Bayesian optimisation is applied to investigate the width and depth and select the best refining method to train the weak learner, i.e. boosting, or the effectiveness of ensemble aggregation method, i.e. bagging.

The quantitative topographical characterisation results, obtained according to the methodology presented in Section 2.2, are exploited to train the supervised machine learning classifier. Training and classification are performed in Matlab 2019b.

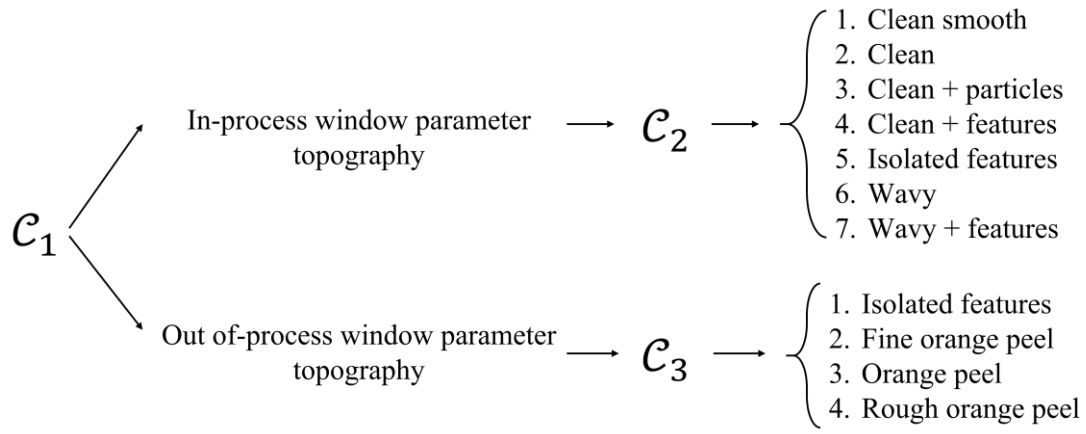

Figure 2 Surface topography classifier workflow.

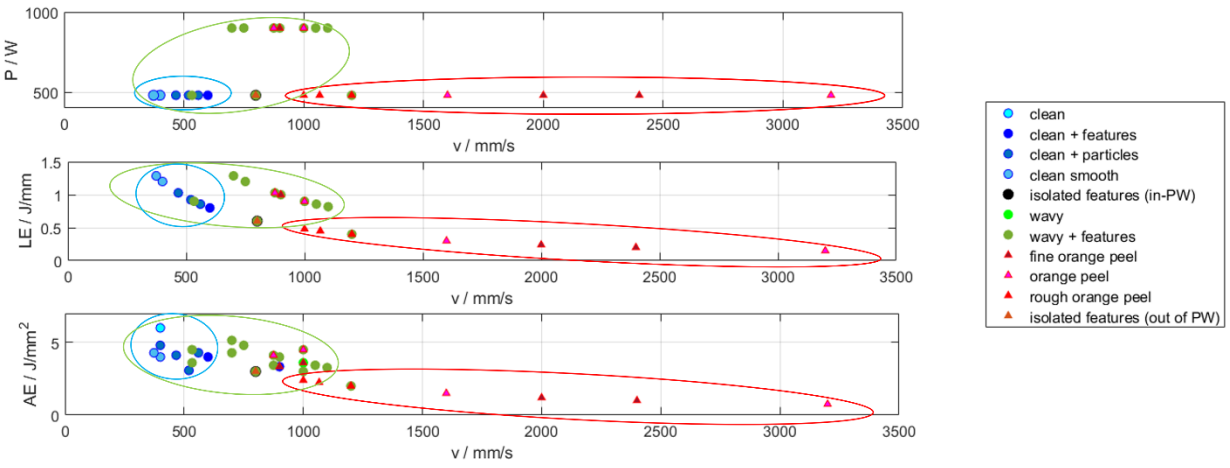

Figure 3 Power (P), Line Energy (LE) and Area Energy (AE) as a function of the scanning speed (v). Data points are classified on the basis of the topographical classes and clustered on the basis of process parameters window (PW), i.e. out of process window (red

ellipsis) and in-process window (green). According to the literature, an optimized process condition (blue ellipsis) can also be identified, considering further properties, e.g. porosity [46].

3. RESULTS AND DISCUSSION

3.1 Topographical and morphological characterisation

Table A 1 summarises the results of the topographical characterisation, highlighting the class type as per Section 2.2. Figure 1 shows low magnification images of the samples' top surface obtained with a stereomicroscope with an 8× magnification. As intended, the considered range of process parameters allowed generating the main classes of topographies that can be obtained, according to literature, under different process conditions. Insights are shown in Figure 4 and Figure 5, which report the SEM image and the pseudo-colour map resulting from the CSI topographical measurement.

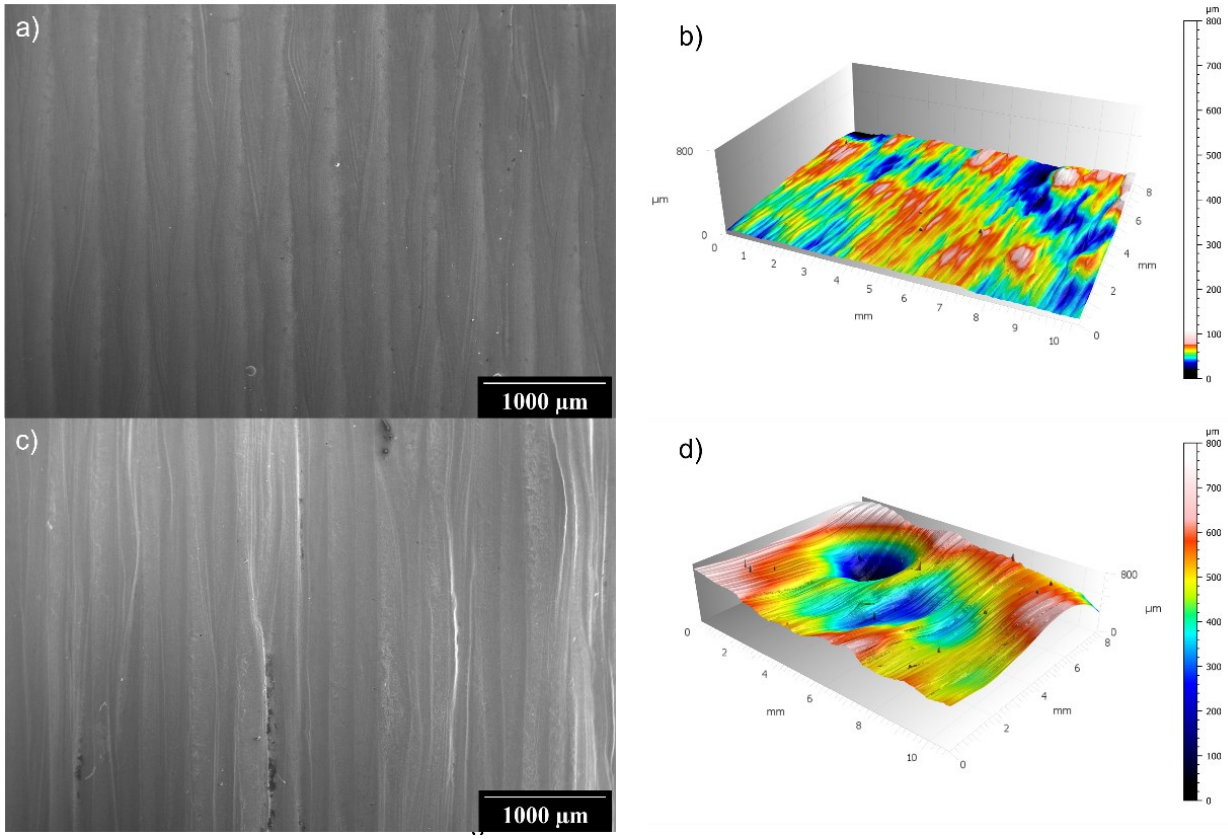

Figure 4 Example of in-process parameter window as-built surface topography of H13 by EB-PBF. Clean surface measured by (a) SEM at 55x magnification and (b) by CSI. Wavy topography measured by (c) SEM at 55x magnification and (d) by CSI. Scanning tracks can be appreciated on both topographies. Notice that the vertical scale range is the same to stress the comparison.

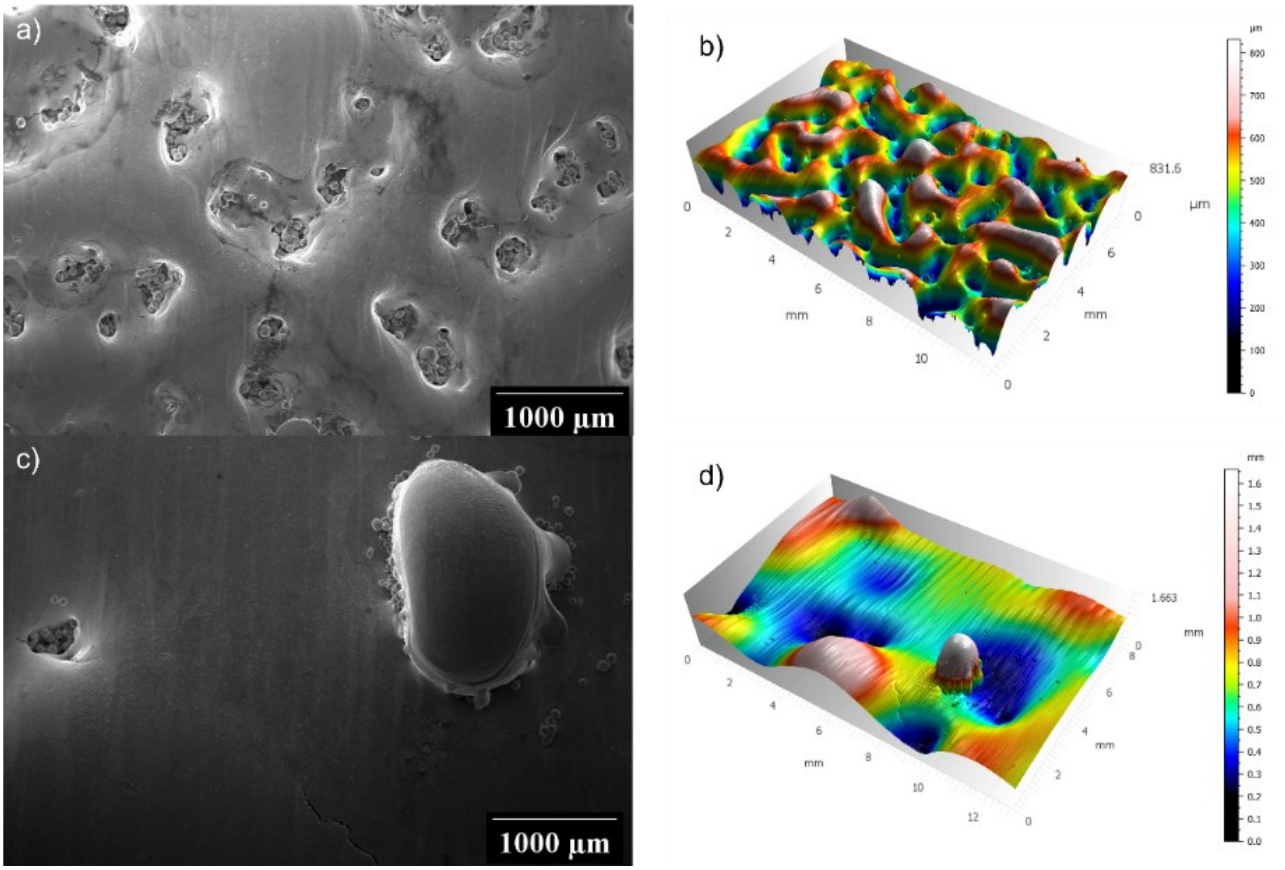

Figure 5 Example of surface topography of H13 by EB-PBF in non-optimised process condition. Orange peel surface measured by (a) SEM at 55x magnification and (b) by CSI. Notice the unmelted powder particles entrapped in the surface pores. Wavy topography with features measured by (c) SEM at 55x magnification and (d) by CSI. Both small surface pores with entrapped unmelted powder particles with fine particle size and a relevant globule with satellite sputter and powder particles. (c, d) Appreciate also the presence of a crack at the centre of lower longer side.

3.2 Supervised Machine Learning classification

The dataset of Table A 1 is exploited to train the classifier according to the methodology of Section 2.3. The Bayesian optimisation with 45 iterations selected as the first classifier $\mathcal{C}_1$ a SVM with a quadratic kernel and a tolerance ϵ of 0.26. Figure 6(a) shows the related Bayesian optimisation graph that plots the evolution of the misclassification error forecast with the (updated) prior and the actual observed value at each iteration (exploited to evaluate the posterior). The graph highlights that the number of iterations was sufficient to select the best set of hyperparameters. Additionally, the graph shows the iteration in which the set of hyperparameters yielding the minimum classification error is achieved and the one in which the minimum upper bound of the misclassification error, useful information for the acquisition function. The cross-validation results in an average accuracy of the selected classifier $\mathcal{C}_1$ for the considered case study of 100% as shown by the confusion matrix reported in Figure 6(b).

The two groups of data are then exploited to train the classifiers $\mathcal{C}_2$ and $\mathcal{C}_3$. In both cases, the Bayesian optimisation selected a bagged classifier, with main hyperparameters summarised respectively in Figure 7(a) and Figure 8(a). The cross-validation results in an average trained classifiers' accuracy of 84.4% and 90.6% due to the confusion matrix shown in Figure 7(b) and Figure 8(b), respectively, resulting in an overall accuracy of the classifier $\mathcal{C}$ of 87%.

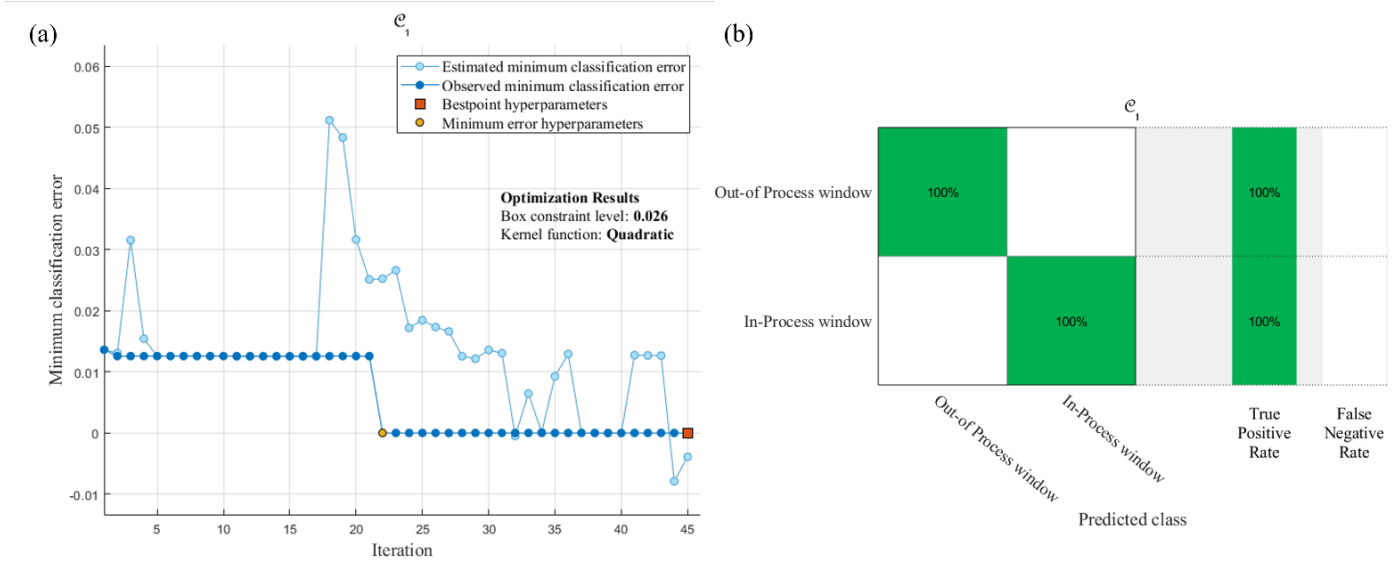

Figure 6 (a) Plot of minimum classification error evolution during the Bayesian optimisation of the classifier $\mathcal{C}_1$. (b) Confusion matrix of the optimised classifier.

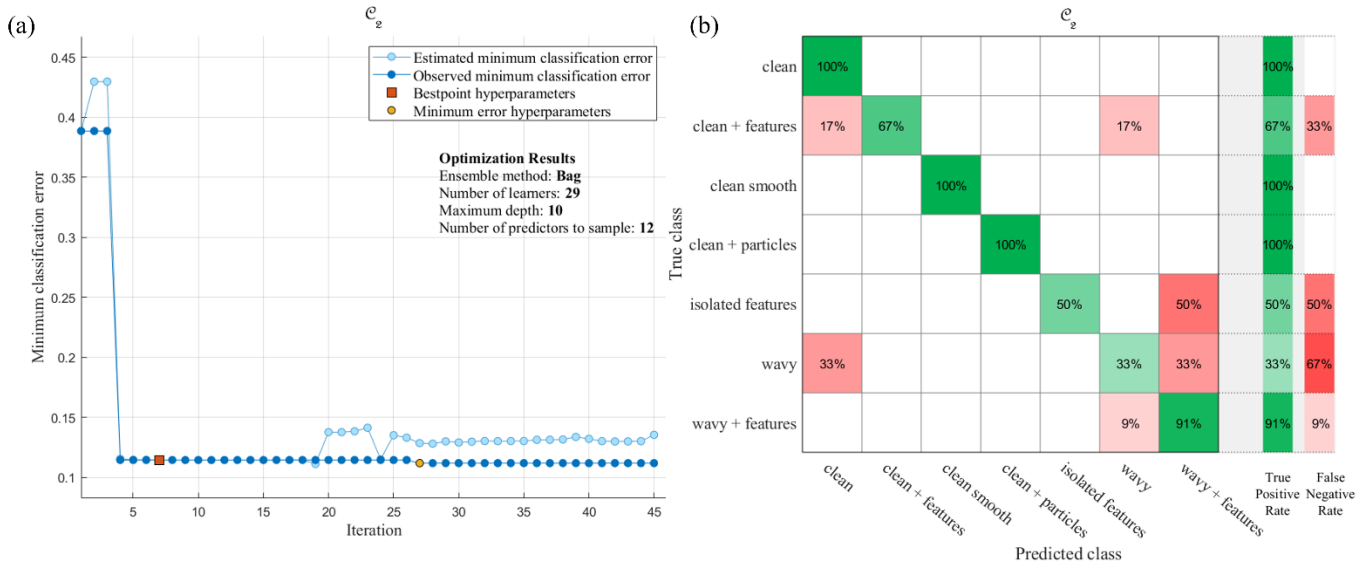

Figure 7 (a) Plot of minimum classification error evolution during the Bayesian optimisation of the classifier $\mathcal{C}_2$. (b) Confusion matrix of the optimised classifier.

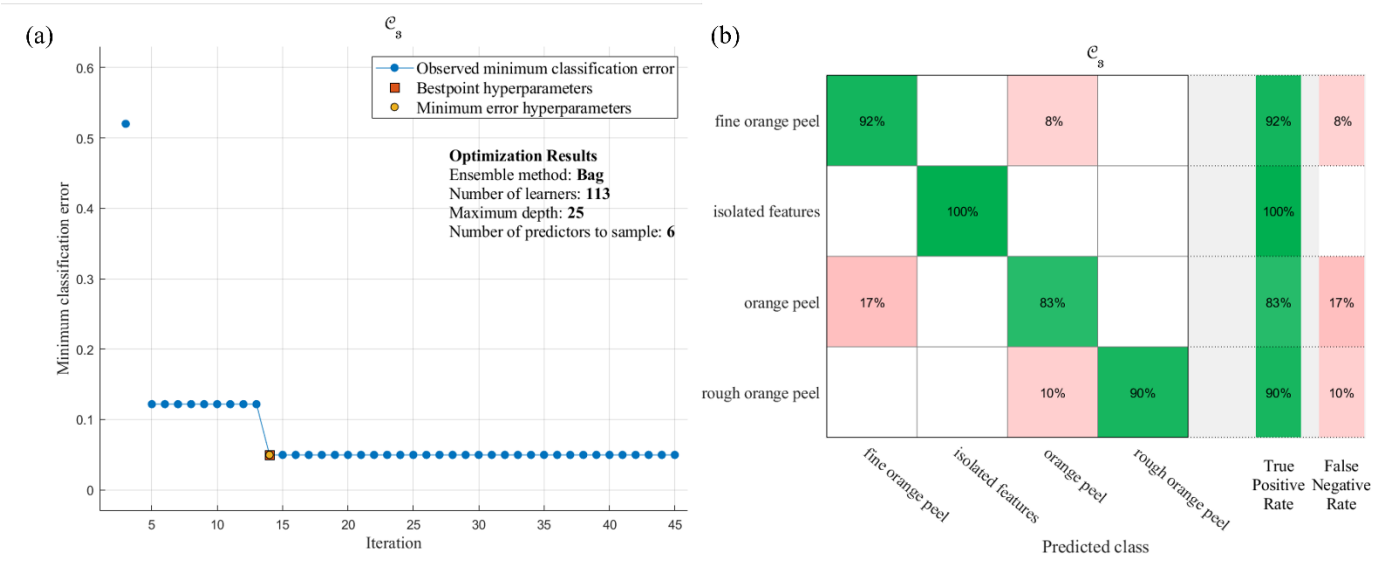

Figure 8 (a) Plot of minimum classification error evolution during the Bayesian optimisation of the classifier $\mathcal{C}_3$. (b) Confusion matrix of the optimised classifier.

3.3 Discussion

According to the literature, the process conditions generated an exhaustive set of possible topographies [13,44,45,62,63]. Clean and wavy topographies, generated with process parameters inside the process window, feature a distinctive regular texture due to the process signature, i.e. the scanning tracks; see Figure 4(a) and Figure 4(c), respectively. Conversely, process set-up significantly far from the best conditions in the process window induces either orange peel topography or the presence of significant features. The SEM analysis shows that the generated surface pores are filled with unmelted powder particles with a fine powder particle size (significantly smaller than 100 µm), which tend to agglomerate at the ridge of large isolated swollen area, identified as globules.

The topographies were quantitatively characterised through a complex set of field and feature topographical parameters [43,62,79]. Amongst these, contrary to the common practice of only reporting *Sa* and *Sz*, *Sq* and *Sdq* appear to be highly indicative of the change in surface topography. With process parameters out of the process window, orange peel topographies are generated. These are entirely dominated by surface pores and quantified well by the $A_{\%p}$.

The generated dataset, reported in Table A 1, is exploited to train the proposed classifier, whose structure is shown in Figure 2, and whose hyperparameters are selected by Bayesian optimisation. The obtained result achieves a satisfactory overall accuracy of 87%. In the first step, binary classification is obtained by a quadratic SVM, with accurate and precise performances. The second step of classification in topographical classes is more complex due to the higher number of alternatives. Bagged ensembles of CART classifiers solve the classification problem with satisfactory results. The confusion matrixes show that misclassifications are committed in neighbouring classes and consequently are not severe. For example, 17% of clean topographies with features are confused with clean topographies, i.e. suggesting that the present features have a marginal contribution to the parameters. Similarly, 8% of fine orange peel topographies are confused with the orange peel type. Accuracy of prediction is satisfactory also considering the repeatability of the process when parameters are inside the process window [43,104]. Misclassifications arise when parameters are either out of the process window (see Figure 8) or approaching it, e.g. more complex topographies resulting from nominally in-process window parameters (see Figure 7). This is consistent with the increasing amount of complex interactions elicited by such conditions. However, as far as quality inspections are concerned, such errors are marginal, since no defective surface is identified as coming from an in process window (see Figure 6). Additionally, those misclassifications could be easily relieved when considering information-rich process control exploiting multi-sensor data-fusion [9].

Indeed, the proposed classifier in Figure 2 is not the unique solution to the problem at hand. An alternative approach consisting of a unique algorithm, $y = \boldsymbol{C}_*(\boldsymbol{x}, \boldsymbol{\vartheta})$, was considered. However, although several supervised machine learning algorithms were tested and optimised, e.g. multinomial logistic regression, naïve bayes classifier, CART and ensembles, none could even achieve an accuracy of 65%. Explanations can be manifold and lay both in the high dimensionality of the studied problem and in the adequacy of the classification algorithm. Conversely, deconstructing the problem into three subproblems aids in identifying and training the most suitable supervised machine learning algorithms.

The high dimensionality of the considered problem was also addressed. While outlining the methodology to characterise PBF as-built topographies [42,58], the literature acknowledges the complexity and large numerosity of the necessary set of parameters, reported in Table 2. Thus, the feature selection problem was addressed to reduce the dimensionality of the classification [105]. None of the applied statistical approaches disproved the hypothesis of statistical significance of the parameters allowing the reduction of the dimensionality.

4. CONCLUSIONS

This paper developed a machine learning classifier of as-built surface topographies by additive manufacturing based on quantitative surface characterization. This is unprecedented in literature, which mostly relies on qualitative classifications. Surface topography characterisation is essential for components due to the correlation with technological properties and functionality. Accordingly, several studies correlated process parameters, topography and parts' properties for PBF processes. These supported the development of in-situ measurement techniques to enable automated and integrated process quality control, some of which measure surface topographies. This work developed a methodology to build a supervised machine learning algorithm to classify the visual aspect of as-built surface topographies based on topographical parameters. The methodology was successfully applied to an industrially relevant case study. The relevance of the algorithm is manifold on the route towards an integrated multi-sensor automated control system for AM. First, it draws a connection between the large set of topographical parameters, which are needed to characterise the surface quantitatively and on the basis of which GD&T are specified, and the visual aspect of the surface, which is of more immediate understanding. Therefore, it can aid component designers in the early phase of design. The second, it will enable, when integrated with current in-situ measurements, mostly based on qualitative inspection, multi-scale, information-rich quality control. Thus, it will augment in-situ measurements informativeness and couple them to quantitative characterisation. The third, it allows for predicting the visual appearance of components based on process parameters, provided a correlation is available. This will aid process designers in setting up and optimising processes more efficiently for new materials and facilitate real-time process parameters control. Future works will tackle the limitations of the proposed methodology by investigating the generalisation of the classifier to include several materials, exploit multi-sensor data, and rely upon unsupervised machine learning to improve performances further. Additionally, future work may exploit the presented methodology to identify other non-standard surface topography parameters, which may improve classification performances.

Acknowledgements

This work has been partially supported by "Ministero dell'Istruzione, dell'Università e della Ricerca". Award "TESUN- 83486178370409 finanziamento dipartimenti di eccellenza CAP. 1694 TIT. 232 ART. 6". The authors would like to thank Dr. Saboori Abdollah, Politecnico di Torino – DIGEP and IAM@PoliTO (Integrated Additive Manufacturing centre of Politecnico di Torino), for the fabrication of EB-PBF specimens, and Prof. Raffaello Levi for the fruitful discussion.

Annex

Table A 1 Results of topographical characterisation of the 52 considered samples. Data from 53rd to the 77th refer to samples 1 to 25, measured at the centre of the sample.

Sample #	SRC / µm	Sa / µm	Sq / µm	Sdq	V_g / mm³	$A_{\%g}$ / %	V_p / mm³	$A_{\%p}$ / %	Type
1	4638.00	103	127.4	0.109	8.346	37.39	1.300	29.76	wavy + features
2	1120.00	54.74	67.9	0.222	0.000	0.00	4.673	100.00	orange peel
3	617.00	49.33	62.4	0.296	1.476	20.61	2.235	79.39	orange peel
4	402.30	61.24	77.38	0.373	0.204	2.14	3.210	97.86	orange peel
5	906.30	48.96	62.57	0.228	0.743	6.25	3.336	93.75	orange peel
6	926.60	44.07	54.99	0.074	0.279	4.80	0.184	20.44	clean + features
7	1607.00	66.39	81.08	0.211	0.000	0.00	6.914	100.00	orange peel
8	1020.00	58.3	72.48	0.244	1.956	16.81	3.592	83.19	orange peel
9	2006.00	54.97	70.33	0.113	4.160	28.08	4.384	71.92	isolated features
10	3151.00	31.24	37.43	0.034	3.206	21.98	0.368	26.79	clean + features
11	1957.00	63.73	77.23	0.146	0.000	0.00	6.393	100.00	isolated features
12	1265.00	93.79	110.8	0.288	0.000	0.00	3.851	100.00	orange peel
13	2113.00	76.31	93.9	0.209	0.000	0.00	8.182	100.00	orange peel
14	1301.00	64.24	79.86	0.236	0.686	3.99	5.761	96.01	orange peel
15	1829.00	74.12	89.66	0.082	1.736	8.68	0.362	18.56	clean + features
16	4656.00	100.8	119.7	0.095	9.365	47.22	1.119	30.09	wavy + features
17	1064.00	56.34	70.74	0.220	1.527	10.86	3.724	89.14	orange peel
18	3336.00	140.7	177.7	0.146	5.080	37.82	1.187	29.52	wavy + features
19	677.30	50.42	64.74	0.257	1.638	19.78	2.359	80.21	orange peel
20	759.70	49.71	63.7	0.256	0.955	7.75	3.373	92.25	orange peel
21	430.20	54.74	67.33	0.068	0.000	0.00	0.000	0.00	clean
22	1414.00	61.21	76.5	0.136	0.000	0.00	1.226	57.97	isolated features

23	1319.00	59.61	75.35	0.212	0.000	0.00	6.437	100.00	orange peel
24	763.70	52.71	64.58	0.276	0.650	6.87	3.552	93.13	orange peel
25	2738.00	113.2	131.1	0.104	2.045	19.58	0.614	29.20	wavy + features
26	719.00	16.23	21.12	0.053	0.291	10.40	0.000	0.00	clean + particles
27	228.00	8.99	11.39	0.043	0.000	0.00	0.000	0.00	clean smooth
28	221.30	17.75	24.7	0.075	0.007	0.56	0.000	0.00	clean smooth
29	1016.00	10.72	14.35	0.029	0.185	2.61	0.000	0.00	clean + particles
30	781.30	16.16	21.28	0.037	0.107	4.29	0.000	0.00	clean + particles
31	770.70	22.76	27.71	0.046	0.095	0.87	0.000	0.00	clean + particles
32	490.90	10.09	12.86	0.035	0.000	0.00	0.000	0.00	clean smooth
33	1051.00	22.13	27.66	0.051	0.408	2.93	0.000	0.00	clean + particles
34	1006.00	21.62	28.1	0.065	0.875	4.27	0.042	0.58	clean + particles
35	4772.00	145.1	176.1	0.127	0.550	7.43	3.383	21.54	wavy + features
36	4851.00	202.3	242.7	0.145	0.232	3.87	2.630	25.83	wavy + features
37	636.90	152.3	182.6	0.156	0.207	1.04	0.000	0.00	wavy + features
38	1470.00	147	179.6	0.163	0.788	9.77	0.294	10.72	wavy + features
39	789.90	173.4	235.1	0.231	0.862	6.89	0.136	7.60	wavy + features
40	3736.00	96.33	125.1	0.106	0.492	4.58	1.374	15.95	wavy + features
41	3205.00	101.8	125.5	0.106	0.129	0.57	1.283	13.14	wavy + features
42	2018.00	122.4	156.6	0.126	0.339	6.88	0.537	10.17	wavy + features
43	1095.00	152.3	192.1	0.171	0.939	6.53	0.221	6.56	wavy + features
44	3284.00	187.3	218.8	0.196	0.318	5.98	8.964	52.91	wavy + features
45	3361.00	57.01	69.41	0.061	0.255	9.14	2.054	31.28	wavy
46	4564.00	78.51	92.12	0.064	0.520	4.99	4.917	32.39	wavy + features
47	3118.00	159.1	185.2	0.189	0.126	4.07	5.780	36.96	wavy + features
48	3231.00	63.59	77.02	0.058	0.095	6.37	0.498	20.48	wavy

49	7846.00	56.2	65.69	0.029	2.870	25.76	2.185	16.00	wavy + features
50	3606.00	186.2	217	0.145	1.150	11.51	3.979	33.36	wavy + features
51	1263.00	224.4	275.8	0.305	0.396	8.95	1.951	21.64	wavy + features
52	4564.00	78.51	92.12	0.064	0.544	5.76	4.792	29.64	wavy
53	3950.00	82.27	95.58	0.085	10.150	51.71	0.053	3.14	wavy + features
54	1112.00	61.49	77.42	0.256	0.000	0.00	4.639	100.00	orange peel
55	595.00	53.44	69.99	0.319	1.652	35.73	7.280	79.39	orange peel
56	402.30	61.24	77.38	0.373	0.204	2.14	3.210	97.86	orange peel
57	882.40	49.17	61.2	0.212	1.297	1.06	2.448	48.42	orange peel
58	1003.00	52.58	65.86	0.089	0.000	0.00	2.084	7.28	clean + features
59	1323.00	78.24	93.8	0.263	3.462	4.08	4.426	95.92	orange peel
60	871.90	62.02	77.43	0.278	1.644	16.40	2.876	83.60	orange peel
61	1500.00	52.48	63.61	0.137	2.135	15.82	3.528	52.13	isolated features
62	3150.80	31.1	37.28	0.030	3.206	21.98	0.368	26.79	clean + features
63	1654.00	72.1	86.41	0.167	0.000	0.00	4.095	100.00	isolated features
64	1265.00	93.79	110.8	0.288	0.000	0.00	3.851	100.00	orange peel
65	1564.00	84.77	103.6	0.233	0.301	1.61	4.526	98.39	orange peel
66	1183.00	66.43	81.33	0.251	0.000	0.00	4.482	100.00	orange peel
67	3205.00	33.07	43.06	0.039	2.592	12.80	0.000	0.00	clean + features
68	3324.00	103.7	120.9	0.099	5.163	55.75	0.000	0.00	wavy + features
69	1131.00	54.95	70.25	0.203	1.787	15.83	3.165	84.17	orange peel
70	5588.00	95.38	130.4	0.104	12.130	84.86	0.152	7.06	wavy + features
71	630.00	57.5	74.09	0.303	1.413	21.47	2.081	67.39	orange peel
72	681.40	57.75	75.64	0.284	0.299	4.30	2.751	95.70	orange peel
73	503.50	57.2	70.35	0.066	0.000	0.00	0.000	0.00	clean
74	792.30	82.37	102.7	0.136	0.000	0.00	0.696	17.97	isolated features

75	1382.00	55.62	67.4	0.200	0.000	0.00	4.690	100.00	orange peel
76	824.50	50.85	63.89	0.254	0.770	9.07	2.869	90.93	orange peel
77	3530.00	134.7	172.2	0.139	1.435	11.75	0.257	5.59	wavy + features

Bibliography

[1] P. Zheng, H. wang, Z. Sang, R.Y. Zhong, Y. Liu, C. Liu, K. Mubarok, S. Yu, X. Xu, Smart manufacturing systems for Industry 4.0: Conceptual framework, scenarios, and future perspectives, Front. Mech. Eng. 13 (2018) 137–150. https://doi.org/10.1007/s11465-018-0499-5.

[2] J. Butt, Exploring the Interrelationship between Additive, (2020) 1–33.

[3] H. Parmar, T. Khan, F. Tucci, R. Umer, P. Carlone, Advanced robotics and additive manufacturing of composites: towards a new era in Industry 4.0, Mater. Manuf. Process. 00 (2021) 1–35. https://doi.org/10.1080/10426914.2020.1866195.

[4] M.K. Thompson, G. Moroni, T. Vaneker, G. Fadel, R.I. Campbell, I. Gibson, A. Bernard, J. Schulz, P. Graf, B. Ahuja, F. Martina, Design for Additive Manufacturing: Trends, opportunities, considerations, and constraints, CIRP Ann. 65 (2016) 737–760. https://doi.org/10.1016/j.cirp.2016.05.004.

[5] K. Kellens, M. Baumers, T.G. Gutowski, W. Flanagan, R. Lifset, J.R. Duflou, Environmental Dimensions of Additive Manufacturing: Mapping Application Domains and Their Environmental Implications, J. Ind. Ecol. 21 (2017) S49–S68. https://doi.org/10.1111/jiec.12629.

[6] T. Peng, K. Kellens, R. Tang, C. Chen, G. Chen, Sustainability of additive manufacturing: An overview on its energy demand and environmental impact, Addit. Manuf. 21 (2018) 694–704. https://doi.org/10.1016/j.addma.2018.04.022.

[7] EC Joint Research Centre, Critical Raw Materials for Strategic Technologies and Sectors in the EU - a Foresight Study, EU, Luxembourgh, 2020. https://doi.org/10.2873/58081.

[8] A. Iqbal, G. Zhao, H. Suhaimi, N. He, G. Hussain, W. Zhao, Readiness of subtractive and additive manufacturing and their sustainable amalgamation from the perspective of Industry 4.0: a comprehensive review, Int. J. Adv. Manuf. Technol. 111 (2020) 2475–2498. https://doi.org/10.1007/s00170-020-06287-6.

[9] M. Grasso, A. Remani, A. Dickins, B.M. Colosimo, R.K. Leach, In-situ measurement and monitoring methods for metal powder bed fusion – an updated review, Meas. Sci. Technol. 32 (2021) 112001.

[10] I. Gibson, D. Rosen, B. Stucker, Additive manufacturing technologies, (2010).

[11] L.E. Murr, S.M. Gaytan, Electron Beam Melting, Elsevier, 2014. https://doi.org/10.1016/B978-0-08-096532-1.01004-9.

[12] C. Körner, Additive manufacturing of metallic components by selective electron beam melting - A review, Int. Mater. Rev. 61 (2016) 361–377. https://doi.org/10.1080/09506608.2016.1176289.

[13] C. Guo, W. Ge, F. Lin, Effects of scanning parameters on material deposition during Electron Beam Selective Melting of Ti-6Al-4V powder, J. Mater. Process. Technol. 217 (2015) 148–157. https://doi.org/10.1016/j.jmatprotec.2014.11.010.

[14] P. Wang, W.J. Sin, M.L.S. Nai, J. Wei, Effects of processing parameters on surface roughness of additive manufactured Ti-6Al-4V via electron beam melting, Materials (Basel). 10 (2017) 8–14. https://doi.org/10.3390/ma10101121.

[15] L.E. Murr, A Metallographic Review of 3D Printing/Additive Manufacturing of Metal and Alloy Products and Components, Metallogr. Microstruct. Anal. 7 (2018) 103–132.

https://doi.org/10.1007/s13632-018-0433-6.

[16] X.P. Ren, H.Q. Li, H. Guo, F.L. Shen, C.X. Qin, E.T. Zhao, X.Y. Fang, A comparative study on mechanical properties of Ti–6Al–4V alloy processed by additive manufacturing vs. traditional processing, Mater. Sci. Eng. A. 817 (2021). https://doi.org/10.1016/j.msea.2021.141384.

[17] L.M. Sochalski-Kolbus, E.A. Payzant, P.A. Cornwell, T.R. Watkins, S.S. Babu, R.R. Dehoff, M. Lorenz, O. Ovchinnikova, C. Duty, Comparison of Residual Stresses in Inconel 718 Simple Parts Made by Electron Beam Melting and Direct Laser Metal Sintering, Metall. Mater. Trans. A. 46 (2015) 1419–1432. https://doi.org/10.1007/s11661-014-2722-2.

[18] M. Galati, G. Rizza, A. Salmi, S. Biamino, C. Ghibaudo, P. Fino, L. Iuliano, Residual stress investigation on Ti-48Al-2Cr-2Nb samples produced by Electron Beam Melting process, Procedia CIRP. 99 (2021) 336–341. https://doi.org/10.1016/j.procir.2021.03.049.

[19] N. Li, S. Huang, G. Zhang, R. Qin, W. Liu, H. Xiong, G. Shi, J. Blackburn, Progress in additive manufacturing on new materials: A review, J. Mater. Sci. Technol. 35 (2019) 242–269. https://doi.org/10.1016/j.jmst.2018.09.002.

[20] P. Fernandez-Zelaia, C. Ledford, E.A.I. Ellis, Q. Campbell, A.M. Rossy, D.N. Leonard, M.M. Kirka, Crystallographic texture evolution in electron beam melting additive manufacturing of pure Molybdenum, Mater. Des. 207 (2021) 109809. https://doi.org/10.1016/j.matdes.2021.109809.

[21] E.A.I. Ellis, M.A. Sprayberry, C. Ledford, J.P. Hankwitz, M.M. Kirka, C.D. Rock, T.J. Horn, Y. Katoh, R.R. Dehoff, Processing of tungsten through electron beam melting, J. Nucl. Mater. 555 (2021) 153041. https://doi.org/10.1016/j.jnucmat.2021.153041.

[22] V. Güther, M. Allen, J. Klose, H. Clemens, Metallurgical processing of titanium aluminides on industrial scale, Intermetallics. 103 (2018) 12–22. https://doi.org/10.1016/j.intermet.2018.09.006.

[23] A. Ostovari Moghaddam, N.A. Shaburova, M.N. Samodurova, A. Abdollahzadeh, E.A. Trofimov, Additive manufacturing of high entropy alloys: A practical review, J. Mater. Sci. Technol. 77 (2021) 131–162. https://doi.org/10.1016/j.jmst.2020.11.029.

[24] N. Hrabe, T. Quinn, Effects of processing on microstructure and mechanical properties of a titanium alloy (Ti-6Al-4V) fabricated using electron beam melting (EBM), Part 2: Energy input, orientation, and location, Mater. Sci. Eng. A. 573 (2013) 271–277. https://doi.org/10.1016/j.msea.2013.02.065.

[25] H. Bian, K. Aoyagi, Y. Zhao, C. Maeda, T. Mouri, A. Chiba, Microstructure refinement for superior ductility of Al–Si alloy by electron beam melting, Addit. Manuf. 32 (2020) 100982. https://doi.org/10.1016/j.addma.2019.100982.

[26] D. Cormier, O. Harrysson, J. Low, K. Knowlson, Optimization of the electron beam melting process, IIE Annu. Conf. Exhib. 2004. (2004) 733–738.

[27] H. Gong, K. Rafi, H. Gu, G.D. Janaki Ram, T. Starr, B. Stucker, Influence of defects on mechanical properties of Ti-6Al-4V components produced by selective laser melting and electron beam melting, Mater. Des. 86 (2015) 545–554. https://doi.org/10.1016/j.matdes.2015.07.147.

[28] A. Safdar, H.Z. He, L.Y. Wei, A. Snis, L.E. Chavez De Paz, Effect of process parameters settings and thickness on surface roughness of EBM produced Ti-6Al-4V, Rapid Prototyp. J. 18 (2012) 401–408. https://doi.org/10.1108/13552541211250391.

[29] R. Leach, S. Carmignato, Precision Metal Additive Manufacturing, 2020. https://doi.org/10.1201/9780429436543.

[30] H. Gong, K. Rafi, N. V Karthik, T. Starr, B. Stucker, Defect morphology in Ti-6Al-4V Parts Fabricated by Selective Laser Melting and Electron Beam Melting, 24th Annu. Int. Solid Free. Fabr. Symp. (2013) 440–453. https://doi.org/DOI: 10.1007/s11665-013-0658-0.

[31] S. Biamino, A. Penna, U. Ackelid, S. Sabbadini, O. Tassa, P. Fino, M. Pavese, P. Gennaro, C. Badini, Electron beam melting of Ti-48Al-2Cr-2Nb alloy: Microstructure and mechanical properties

investigation, Intermetallics. 19 (2011) 776–781. https://doi.org/10.1016/j.intermet.2010.11.017.

[32] G. Maculotti, G. Genta, M. Lorusso, M. Galetto, Assessment of heat treatment effect on AlSi10Mg by selective laser melting through indentation testing, 2019. https://doi.org/10.4028/www.scientific.net/KEM.813.171.

[33] F.C.M.L. F Trevisan, On the selective laser melting (SLM) of the AlSi10Mg alloy: Process, microstructure, and mechanical properties, Mater. 10 (2017) 76.

[34] M. Galetto, G. Genta, G. Maculotti, E. Verna, Defect Probability Estimation for Hardness-Optimised Parts by Selective Laser Melting, Int. J. Precis. Eng. Manuf. 21 (2020) 1739–1753. https://doi.org/10.1007/s12541-020-00381-1.

[35] A. du Plessis, S. Beretta, Killer notches: The effect of as-built surface roughness on fatigue failure in AlSi10Mg produced by laser powder bed fusion, Addit. Manuf. 35 (2020) 101424. https://doi.org/10.1016/j.addma.2020.101424.

[36] A. Thompson, I. Maskery, R.K. Leach, X-ray computed tomography for additive manufacturing: A review, Meas. Sci. Technol. 27 (2016). https://doi.org/10.1088/0957-0233/27/7/072001.

[37] R.K. Leach, Characterisation of Areal Surface Texture, Springer, Berlin, 2013. https://doi.org/10.1007/978-3-642-36458-7.

[38] A.A.G. Bruzzone, H.L. Costa, P.M. Lonardo, D.A. Lucca, Advances in engineered surfaces for functional performance, CIRP Ann. - Manuf. Technol. 57 (2008) 750–769. https://doi.org/10.1016/j.cirp.2008.09.003.

[39] C.J. Evans, J.B. Bryan, `Structured', `textured' or `engineered' surfaces, CIRP Ann. - Manuf. Technol. 48 (1999) 541–556. https://doi.org/10.1016/S0007-8506(07)63233-8.

[40] G. Maculotti, Advanced Methods for the Mechanical and Topographical Characterization of Technological Surfaces, Politecnico di Torino, 2021.

[41] S. Yoder, P. Nandwana, V. Paquit, M. Kirka, A. Scopel, R.R. Dehoff, S.S. Babu, Approach to qualification using E-PBF in-situ process monitoring in Ti-6Al-4V, Addit. Manuf. 28 (2019) 98–106. https://doi.org/10.1016/j.addma.2019.03.021.

[42] A. du Plessis, S. Beretta, Killer notches: The effect of as-built surface roughness on fatigue failure in AlSi10Mg produced by laser powder bed fusion, Addit. Manuf. 35 (2020) 101424. https://doi.org/10.1016/j.addma.2020.101424.

[43] L. Newton, N. Senin, E. Chatzivagiannis, B. Smith, R. Leach, Feature-based characterisation of Ti6Al4V electron beam powder bed fusion surfaces fabricated at different surface orientations, Addit. Manuf. 35 (2020) 101273. https://doi.org/10.1016/j.addma.2020.101273.

[44] A. Mohammad, A.M. Al-Ahmari, A. AlFaify, M.K. Mohammed, Effect of melt parameters on density and surface roughness in electron beam melting of gamma titanium aluminide alloy, Rapid Prototyp. J. 23 (2017) 474–485. https://doi.org/10.1108/RPJ-12-2014-0187.

[45] T. Kurzynowski, M. Madeja, R. Dziedzic, K. Kobiela, The effect of EBM process parameters on porosity and microstructure of Ti-5Al-5Mo-5V-1Cr-1Fe alloy, Scanning. 2019 (2019). https://doi.org/10.1155/2019/2903920.

[46] C. Ghibaudo, G. Maculotti, F. Gobber, A. Saboori, M. Galetto, S. Biamino, D. Ugues, Information-rich quality controls prediction model based on Non-Destructive analysis for porosity determination of AISI H13 produced by Electron Beam Melting, Int. J. Adv. Manuf. Technol. Accepted f (n.d.).

[47] A. Dickins, T. Widjanarko, D. Sims-Waterhouse, A. Thompson, S. Lawes, N. Senin, R. Leach, Multi-view fringe projection system for surface topography measurement during metal powder bed fusion, J. Opt. Soc. Am. A. 37 (2020) B93. https://doi.org/10.1364/josaa.396186.

[48] S. Catalucci, N. Senin, D. Sims-Waterhouse, S. Ziegelmeier, S. Piano, R. Leach, Measurement of

complex freeform additively manufactured parts by structured light and photogrammetry, Meas. J. Int. Meas. Confed. 164 (2020) 108081. https://doi.org/10.1016/j.measurement.2020.108081.

[49] T. Santoso, W.P. Syam, S. Darukumalli, Y. Cai, F. Helmli, X. Luo, R. Leach, On-machine focus variation measurement for micro-scale hybrid surface texture machining, Int. J. Adv. Manuf. Technol. 109 (2020) 2353–2364. https://doi.org/10.1007/s00170-020-05767-z.

[50] L. Tan Phuc, M. Seita, A high-resolution and large field-of-view scanner for in-line characterization of powder bed defects during additive manufacturing, Mater. Des. 164 (2019) 107562. https://doi.org/10.1016/j.matdes.2018.107562.

[51] A. Neef, V. Seyda, D. Herzog, C. Emmelmann, M. Schönleber, M. Kogel-Hollacher, Low coherence interferometry in selective laser melting, Phys. Procedia. 56 (2014) 82–89. https://doi.org/10.1016/j.phpro.2014.08.100.

[52] T.G. Fleming, S.G.L. Nestor, T.R. Allen, M.A. Boukhaled, N.J. Smith, J.M. Fraser, Tracking and controlling the morphology evolution of 3D powder-bed fusion in situ using inline coherent imaging, Addit. Manuf. 32 (2020) 100978. https://doi.org/10.1016/j.addma.2019.100978.

[53] C. Arnold, J. Böhm, C. Körner, In Operando Monitoring by Analysis of Backscattered Electrons during Electron Beam Melting, Adv. Eng. Mater. 22 (2020). https://doi.org/10.1002/adem.201901102.

[54] H. Wong, D. Neary, E. Jones, P. Fox, C. Sutcliffe, Pilot capability evaluation of a feedback electronic imaging system prototype for in-process monitoring in electron beam additive manufacturing, Int. J. Adv. Manuf. Technol. 100 (2019) 707–720. https://doi.org/10.1007/s00170-018-2702-6.

[55] R.K. Leach, Optical Measurement of Surface Topography, Springer, Berlin, 2011.

[56] Y. Chen, X. Peng, L. Kong, G. Dong, A. Remani, R. Leach, Defect inspection technologies for additive manufacturing, Int. J. Extrem. Manuf. 3 (2021). https://doi.org/10.1088/2631-7990/abe0d0.

[57] M. Liu, C. Fai Cheung, N. Senin, S. Wang, R. Su, R. Leach, On-machine surface defect detection using light scattering and deep learning, J. Opt. Soc. Am. A. 37 (2020) B53. https://doi.org/10.1364/josaa.394102.

[58] K. Okarma, J. Fstowicz, Progress in Computer Recognition Systems, Springer International Publishing, Cham, 2020. https://doi.org/10.1007/978-3-030-19738-4.

[59] M. Moretti, A. Rossi, N. Senin, In-process monitoring of part geometry in fused filament fabrication using computer vision and digital twins, Addit. Manuf. 37 (2021) 101609. https://doi.org/10.1016/j.addma.2020.101609.

[60] ISO 25178-2:2012 Geometrical product specifications (GPS) - Surface texture: Areal. Part 2: Terms, definitions and surface texture parameters, n.d.

[61] L. Chen, X. Yao, P. Xu, S.K. Moon, G. Bi, Rapid surface defect identification for additive manufacturing with in-situ point cloud processing and machine learning, Virtual Phys. Prototyp. 16 (2021) 50–67. https://doi.org/10.1080/17452759.2020.1832695.

[62] S. Lou, X. Jiang, W. Sun, W. Zeng, L. Pagani, P.J. Scott, Characterisation methods for powder bed fusion processed surface topography, Precis. Eng. 57 (2019) 1–15. https://doi.org/10.1016/j.precisioneng.2018.09.007.

[63] A. Bauereiß, T. Scharowsky, C. Körner, Defect generation and propagation mechanism during additive manufacturing by selective beam melting, J. Mater. Process. Technol. 214 (2014) 2522–2528. https://doi.org/10.1016/j.jmatprotec.2014.05.002.

[64] N. Senin, R. Leach, Information-rich surface metrology, Procedia CIRP. 75 (2018) 19–26. https://doi.org/10.1016/j.procir.2018.05.003.

[65] G. Maculotti, N. Senin, O. Oyelola, M. Galetto, A. Clare, R. Leach, Multi-sensor data fusion for the characterisation of laser cladded cermet coatings, in: Eur. Soc. Precis. Eng. Nanotechnology, Conf.

Proc. - 19th Int. Conf. Exhib. EUSPEN 2019, 2019.

[66] M. Mazur, P. Brincat, M. Leary, M. Brandt, Numerical and experimental evaluation of a conformally cooled H13 steel injection mould manufactured with selective laser melting, Int. J. Adv. Manuf. Technol. 93 (2017) 881–900. https://doi.org/10.1007/s00170-017-0426-7.

[67] L. Rännar, A. Glad, C. Gustafson, Efficient cooling with tool inserts manufactured by electron beam melting, Rapid Prototyp. J. 13 (2007) 128–135. https://doi.org/10.1108/13552540710750870.

[68] G.J. Gibbons, R.G. Hansell, Direct tool steel injection mould inserts through the Arcam EBM free-form fabrication process, Assem. Autom. 25 (2005) 300–305. https://doi.org/10.1108/01445150510626433.

[69] M. Narvan, K.S. Al-Rubaie, M. Elbestawi, Process-structure-property relationships of AISI H13 tool steel processed with selective laser melting, Materials (Basel). 12 (2019) 1–20. https://doi.org/10.3390/ma12142284.

[70] R. Dörfert, J. Zhang, B. Clausen, H. Freiße, J. Schumacher, F. Vollertsen, Comparison of the fatigue strength between additively and conventionally fabricated tool steel 1.2344, Addit. Manuf. 27 (2019) 217–223. https://doi.org/10.1016/j.addma.2019.01.010.

[71] J. Krell, A. Röttger, K. Geenen, W. Theisen, General investigations on processing tool steel X40CrMoV5-1 with selective laser melting, J. Mater. Process. Technol. 255 (2018) 679–688. https://doi.org/10.1016/j.jmatprotec.2018.01.012.

[72] Y. He, M. Zhong, J. Beuth, B. Webler, A study of microstructure and cracking behavior of H13 tool steel produced by laser powder bed fusion using single-tracks, multi-track pads, and 3D cubes, J. Mater. Process. Technol. 286 (2020) 116802. https://doi.org/10.1016/j.jmatprotec.2020.116802.

[73] M. Yonehara, T.T. Ikeshoji, T. Nagahama, T. Mizoguchi, M. Tano, T. Yoshimi, H. Kyogoku, Parameter optimization of the high-power laser powder bed fusion process for H13 tool steel, Int. J. Adv. Manuf. Technol. 110 (2020) 427–437. https://doi.org/10.1007/s00170-020-05879-6.

[74] M. Katancik, S. Mirzababaei, M. Ghayoor, S. Pasebani, Selective laser melting and tempering of H13 tool steel for rapid tooling applications, J. Alloys Compd. 849 (2020) 156319. https://doi.org/10.1016/j.jallcom.2020.156319.

[75] J. Wang, S. Liu, Y. Fang, Z. He, A short review on selective laser melting of H13 steel, Int. J. Adv. Manuf. Technol. 108 (2020) 2453–2466. https://doi.org/10.1007/s00170-020-05584-4.

[76] R. Mertens, B. Vrancken, N. Holmstock, Y. Kinds, J.P. Kruth, J. Van Humbeeck, Influence of powder bed preheating on microstructure and mechanical properties of H13 tool steel SLM parts, Phys. Procedia. 83 (2016) 882–890. https://doi.org/10.1016/j.phpro.2016.08.092.

[77] D. Cormier, O. Harrysson, H. West, Characterization of H13 steel produced via electron beam melting, Rapid Prototyp. J. 10 (2004) 35–41. https://doi.org/10.1108/13552540410512516.

[78] C. Ghibaudo, A. Saboori, G. Marchese, F. Gobber, S. Biamino, D. Ugues, Preliminary processability evaluation of H13 steel by Electron Beam Melting, in: Euro PM 2021 Congr. Exhib., 2021: p. Accepted for publication.

[79] G. Maculotti, G. Piscopo, G. Marchiandi, E. Atzeni, A. Salmi, L. Iuliano, Build orientation effect on Ti6Al4V thin-wall topography by electron beam powder bed fusion, Procedia CIRP. 108C (2022) 222–227.

[80] G. Maculotti, G. Genta, D. Quagliotti, M. Galetto, H.N. Hansen, Gaussian process regression-based detection and correction of disturbances in surface topography measurements, Qual. Reliab. Eng. Int. (2021) 1–18. https://doi.org/10.1002/qre.2980.

[81] ISO 25178-3:2012 Geometrical product specifications (GPS) — Surface texture: Areal Part 3: Specification operators, (n.d.).

[82] G. Maculotti, X. Feng, R. Su, M. Galetto, R. Leach, Residual flatness and scale calibration for a point

autofocus surface topography measuring instrument, Meas. Sci. Technol. 30 (2019). https://doi.org/10.1088/1361-6501/ab188f.

[83] Z.C. Reese, J.S. Taylor, C.J. Evans, Surface finish metrology of additive-manufactured components, in: ASPE/Euspen 2016 Summer Top. Meet. Dimens. Accuracy Surf. Finish Addit. Manuf., 2016: pp. 50–54.

[84] C.A. Brown, W.A. Johnsen, R.M. Butland, J. Bryan, Scale-Sensitive Fractal Analysis of Turned Surfaces, CIRP Ann. - Manuf. Technol. 45 (1996) 515–518. https://doi.org/10.1016/S0007-8506(07)63114-X.

[85] L. De Chiffre, P. Lonardo, H. Trumpold, D.A. Lucca, G. Goch, C.A. Brown, J. Raja, H.N. Hansen, Quantitative characterization of surface texture, CIRP Ann. - Manuf. Technol. 49 (2000) 635–642. https://doi.org/10.1016/S0007-8506(07)63458-1.

[86] P.J. Scott, Feature parameters, Wear. 266 (2009) 548–551. https://doi.org/10.1016/j.wear.2008.04.056.

[87] N. Senin, A. Thompson, R. Leach, Feature-based characterisation of signature topography in laser powder bed fusion of metals, Meas. Sci. Technol. 29 (2018). https://doi.org/10.1088/1361-6501/aa9e19.

[88] S. Lou, A. Townsend, X. Jiang, L. Blunt, W. Zeng, P. Scott, On characterising surface topography of metal powder bed fusion additive manufactured parts, Proc. 16th Int. Conf. Eur. Soc. Precis. Eng. Nanotechnology, EUSPEN 2016. (2016).

[89] P. de Groot, Coherence Scanning Interferometry, in: R.K. Leach (Ed.), Opt. Meas. Surf. Topogr., Springer-Verlag, Berlin, 2011: pp. 187–208.

[90] ISO 25178-604: 2013 Geometrical product specifications (GPS) — Surface texture : Areal Part 604: Nominal characteristics of non-contact (coherence scanning interferometry) instruments, (n.d.).

[91] C. Gomez, R. Su, A. Thompson, J. DiSciacca, S. Lawes, R. Leach, Optimization of surface measurement for metal additive manufacturing using coherence scanning interferometry, Opt. Eng. 56 (2017) 111714. https://doi.org/10.1117/1.OE.56.11.111714.

[92] N. Senin, A. Thompson, R.K. Leach, Characterisation of the topography of metal additive surface features with different measurement technologies, Meas. Sci. Technol. 28 (2017) 095003.

[93] A. Thompson, N. Senin, C. Giusca, R. Leach, Topography of selectively laser melted surfaces: A comparison of different measurement methods, CIRP Ann. - Manuf. Technol. 66 (2017) 543–546. https://doi.org/10.1016/j.cirp.2017.04.075.

[94] K.P. Murphy, Machine Learning: A Probabilistic Perspective, The MIT Press, Cambridge, MA, 2012. https://doi.org/10.1007/978-94-011-3532-0_2.

[95] L. Breiman, J.H. Friedman, R.A. Olshen, C.J. Stone, Classification and regression trees, Wadsworth Advanced Books and Software, 1984.

[96] L. Breiman, Bagging predictors, Mach. Learn. 24 (1996) 123–140. https://doi.org/10.3390/risks8030083.

[97] L. Breiman, Random forests, Mach. Learn. 45 (2001) 5–32. https://doi.org/10.1201/9780429469275-8.

[98] C. Cortes, V. Vapnik, Support-Vector Networks, Mach. Learn. 20 (1995) 273–297. https://doi.org/10.1111/j.1747-0285.2009.00840.x.

[99] R.E. Schapire, Boosting: Foundations and Algorithms, The MIT Press, 2012. https://doi.org/10.1108/03684921311295547.

[100] T.F. Coleman, Y. Li, A reflective newton method for minimizing a quadratic function subject to bounds on some of the variables, SIAM J. Optim. 6 (1996) 1040–1058.

[101] J. Snoek, H. Larochelle, R.P. Adams, Practical Bayesian optimization of machine learning algorithms, Adv. Neural Inf. Process. Syst. 4 (2012) 2951–2959.

[102] A.D. Bull, Convergence rates of efficient global optimization algorithms, J. Mach. Learn. Res. 12 (2011) 2879–2904.

[103] M.A. Gelbart, J. Snoek, R.P. Adams, Bayesian optimization with unknown constraints, Uncertain. Artif. Intell. - Proc. 30th Conf. UAI 2014. (2014) 250–259.

[104] M. Galati, P. Minetola, G. Rizza, Surface Roughness Characterisation and Analysis of the Electron Beam Melting (EBM) Process, Materials (Basel). 12 (2019) 2211. https://doi.org/10.3390/ma12132211.

[105] M. Kuhn, K. Johnson, Applied predictive modeling, Springer, New York, 2013. https://doi.org/10.1007/978-1-4614-6849-3.